Multiaxis Maglev Positioner With Nanometer Resolution Over Extended Travel Range

Won-jong Kim[1]
Mem. ASME
e-mail: wjkim@tamu.edu

Shobhit Verma

Department of Mechanical Engineering,
Texas A&M University,
College Station, TX 77843-3123

This paper presents a novel multiaxis positioner that operates on the magnetic-levitation (maglev) principle. This maglev stage is capable of positioning at the resolution of a few nanometers over a planar travel range of several millimeters. A novel actuation scheme was developed for the compact design of this stage that enables six-axis force generation with just three permanent magnets. We calculated the forces with electromagnetic analysis over the whole travel range and experimentally verified them with a unit actuator. The single-moving part, namely, the platen, is modeled as a pure mass due to the negligible effect of magnetic spring and damping. There are three laser interferometers and three capacitance sensors to sense the six-axis position/rotation of the platen. A lead-lag compensator was designed and implemented to control each axis. A nonlinear model of the force was developed by electromagnetic analysis, and input current linearization was applied to cancel the nonlinearity of the actuators over the extended travel range. Various experiments were conducted to test positioning and loading capabilities. The 0.267 kg *single-moving platen can carry and precisely position an additional payload of* 2 kg. *Its potential applications include semiconductor manufacturing, microfabrication and assembly, nanoscale profiling, and nanoindentation.* [DOI: 10.1115/1.2789468]

Keywords: nanomanipulation, magnetic levitation, precision positioning, multi-axis motion control, real-time digital control

1 Introduction

Precision positioning and vibration isolation play a crucial role in any research related to manufacturing, manipulation, or scanning applications on the macro- as well as micro-nano levels. Especially, nanopositioning stages need to meet the challenging positioning requirements of the current and future nanotechnology. These positioning stages along with cutting-edge manufacturing technologies will lead to the development of microassemblies and nanostructures. The main objective of these stages is to provide repeatable ultrafine motion capabilities for precision manufacturing systems. The applications of these stages include microstereolithography (μSTL), dip pen nanolithography (DPN), nanoscale profiling, and nanoindentation.

Currently, atomic-level positioning and profiling is accomplished by atomic force microscopes (AFMs) and scanning tunneling microscopes (STMs) [1,2]. Motion capabilities of these devices are limited to a plane with a travel range of hundreds of micrometers and possible several micrometers in the vertical direction. Most actuation units in such stages are based on piezoelectric materials. Piezoelectric actuators have become a standard solution in positioning applications where the displacement must be small. However, piezoelectric actuators are sensitive to environmental changes such as temperature, and nonlinear phenomena of hysteresis and creep affect negatively the dynamic response, sometimes precluding closed-loop operation [3].

A novel positioning technology is required to overcome the limitations of existing techniques and to fulfill the performance specifications for nanomanipulation and nanofabrication processes. Previous research has shown that magnetic levitation is a promising technology for such applications [4–10]. In magnetic-levitation (maglev) stages, there is no mechanical contact between the moving and stationary parts, so there is no mechanical friction, stiction, backlash, and hysteresis that would severely limit the resolution. Jung and Baek presented a 6-DOF (degree-of-freedom) positioner that uses air-core magnetic actuators, a maglev stage that demonstrated a 0.5 μm resolution over a travel range of 32 mm [4]. Kim et al. developed and demonstrated a high-precision planar maglev stage with large planar motion capability, which had 10 nm resolution and 100 Hz control bandwidth [5,6]. Hollis et al. developed a 6-DOF wrist using a maglev technique that was capable of fine motions [7]. A dual-axis repulsive maglev guiding system was developed using permanent magnets [8]. This system used a modified voice-coil motor, a passive carrier, and an active track. Chen et al. designed and developed a planar maglev system for micropositioning with a displacement range of 7 mm and root-mean-square error of 500 nm [9]. Jung developed a 6-DOF magnetic-levitation-driven, automated system for a nondestructive tab inner lead bond quality test system [10]. The stage had a range of 20×20 mm^2 in planar and 1 mm in vertical motions with a resolution on 65 nm as compared to 2 nm in our stage. Our stage is of four times shorter in the travel range but provides 30 times better resolution. Jung's stage weighs 350 g as compared to 267 g of ours. Our stage provides force up to 9 N compared with Jung's single actuator's force up to 1 N [10].

In this paper, we present a new maglev stage that is capable of nanoscale resolution over an extended travel range. This stage, shown in Fig. 1, is based on a novel actuation mechanism in which forces in two perpendicular directions are applied on a single magnet, which reduces the total number of magnets by half and the mass of the moving part. There is only one moving part, namely, the platen, of 0.267 kg. The translational travel range is 5×5 mm^2 in the x-y plane. Due to sensor specifications, this stage is currently limited to move 500 μm in the z axis and 0.1 deg in rotation. However, the mechanical design of the stage makes it capable of rotating more than 5 deg. The actuator force calculation shows that this stage is capable of up to 2.5 g accel-

[1]Corresponding author.

Contributed by the Dynamic Systems, Measurement, and Control Division of ASME for publication in the JOURNAL OF DYNAMIC SYSTEMS MEASUREMENT, AND CONTROL. Manuscript received March 10, 2006; final manuscript received January 23, 2007. Review conducted by Robert Gao.

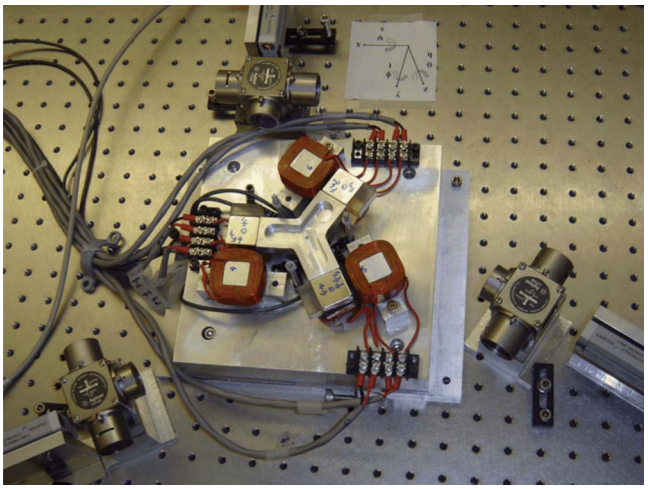

Fig. 1 A photograph of the developed multiaxis maglev positioner

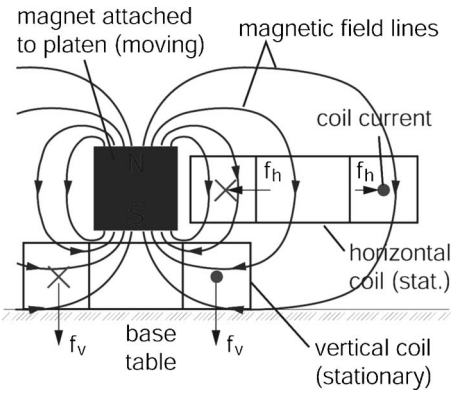

Fig. 2 Cross-sectional side view of the novel dual-axis unit actuator showing magnetic-field lines and directions of forces

eration in the horizontal and 8 g acceleration in the vertical directions. The maximum payload that their actuators can carry is estimated to be 2 kg.

Previously, we developed a six-axis maglev stage capable of 2 nm rms resolution over the travel range of 300 μm in the x, y, and z axes with a payload capacity of 0.3 kg [11,12]. Our current stage presented in this paper has the travel range around 15 times as wide as that of the previous one and the payload capacity of 2 kg as compared to previous 0.3 kg. The nominal power consumption per unit actuator is just 135 mW, less than half of the power consumption of the previous stage, 320 mW. Moreover, the current stage has several additional unique advantages such as fewer parts and no mechanical restriction. There are less than two dozen parts in the whole stage with the minimum number (six) of coils. There are only three magnet pieces, and two coils share the horizontal and vertical magnetic fields of each magnet piece. Due to the absence of any mechanical restriction, the platen can be removed from the machine frame easily without disturbing any stationary parts. This facilitates easy loading and unloading of objects on the platen for various applications. Thus, our new maglev stage possesses competitive advantages in terms of travel range, payload capacity, simplicity in mechanical design, acceleration capability, and power consumption. Although the resolution is currently a bit lower than the previous stage due to nonlineairities in the longer travel range, we expect to improve it with precise modeling and better controllers.

The novelty of this proposed electromagnetic scheme is that it uses the least possible number of magnets and coils to generate all six-axis motions. Here are the comparisons with the three key references [4,9,10]: (1) Jung and Baek [4] used 36 permanent magnets with 25 coils as compared to 3 permanent magnets with 6 coils in our maglev stage. Their calculated positional resolution is 500 nm, i.e., it was the smallest change of motion they could detect considering their sensor range and analog to digital converter (ADC) quantization. We can detect motion as small as 0.6 nm theoretically. (2) Chen et al. [9] used six magnets, and the error in their stage is 500 nm rms as compared to our 4 nm rms. (3) Jung [10] used 16 coils and four permanent magnets on the four ends on a moving part shaped like a plus (+) sign. Minimizing the number of magnets and coils significantly reduces the mechanical complexity for fabrication and modeling. Fewer coils would lead to fewer power-amplifier output channels and make the whole system simple to control.

The maglev stage presented in this paper has been completely manufactured and assembled at Texas A&M University. Its manufacturing cost was less than US$500 excluding sensors and electronics. This paper addresses actuator design and modeling, me-

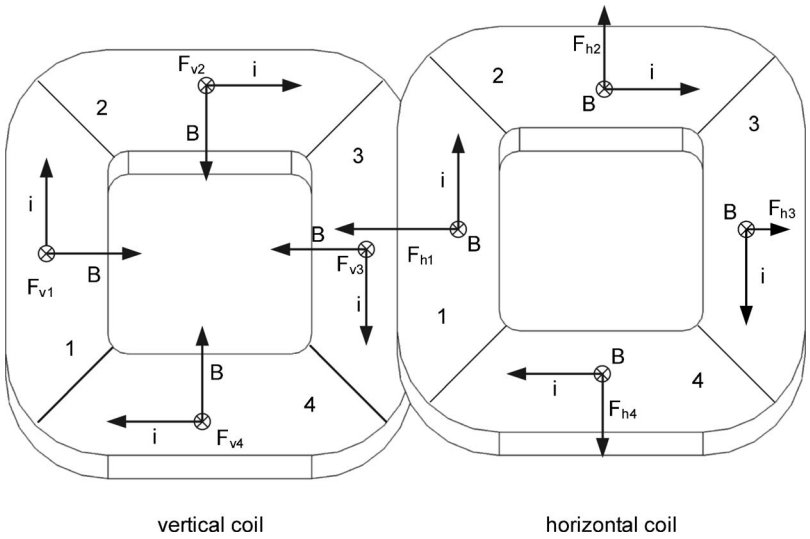

Fig. 3 Top view of the vertical and horizontal coils in a dual-axis actuation system showing the directions of forces on each section of the coils

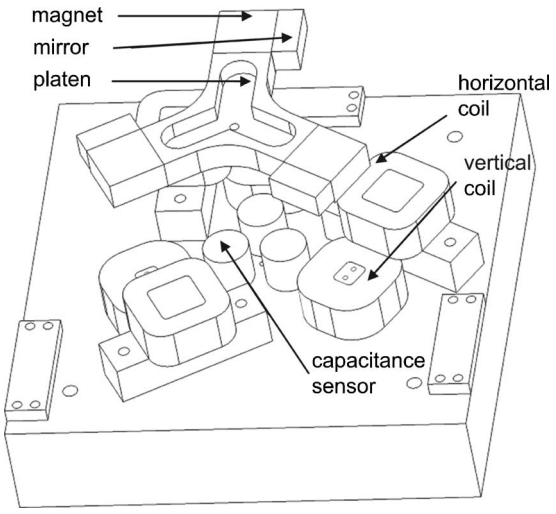

Fig. 4 Exploded view of the assembly of the maglev stage

chanical design and assembly, sensor integration and instrumentation structure, dynamic modeling, and control issues in Secs. 2–5, respectively, and presents extensive experimental results to demonstrate the maglev stage's dynamic performance in Sec. 6.

2 Actuator Design and Modeling

A novel electromagnetic-force-generation scheme was developed to operate this maglev stage. In this section, we present the actuation scheme and analyze the forces.

2.1 Novel Electromagnetic Actuation Scheme. This stage has a Y-shaped moving platen with three identical dual-axis actuation systems at each end. As shown in a cross-sectional side view of the actuation system in Fig. 2 each unit consists of a permanent magnet and two square-shaped coils below and beside the magnet. The magnet is attached to the moving part and the coils are attached to the base plate using coil holders. Figure 2 shows the polarity of the magnet and its magnetic-field lines. Assuming that the direction of the currents (i) in each coil is clockwise seen from the top, the direction of force (F) on each section of the coils is shown in Fig. 3. The magnitude and direction of force are calculated using the Lorentz force, as described in the following section. The length of arrow in Fig. 3 signifies the approximate magnitude of force. The direction of the effective forces can be reversed by reversing the current flow in the coils. We tried to minimize the number of magnets and coils to simplify the mechanical design and to keep the moving part light while maintaining the force capability. In maglev the moving-part mass is a very crucial design factor because a smaller mass requires smaller coil currents to levitate the moving part against gravity. This leads to less power consumption, heat generation, and thermal-expansion error that is detrimental to nanoscale positioning.

2.2 Force Calculation. The force between a current-carrying coil and the permanent magnet is calculated by the Lorentz force law,

$$\mathbf{f} = \int (\mathbf{J} \times \mathbf{B}) dV \tag{1}$$

where $\mathbf{J}$ is the current density (A/m^2) in the coil, $\mathbf{B}$ is the magnetic flux density (T) generated by the permanent magnet, and dV is the small volume segment in the coil. The limits of the volume integral are to cover the whole volume of the coil. The expression of the force acting on the volume (V) of the coil due to the surface

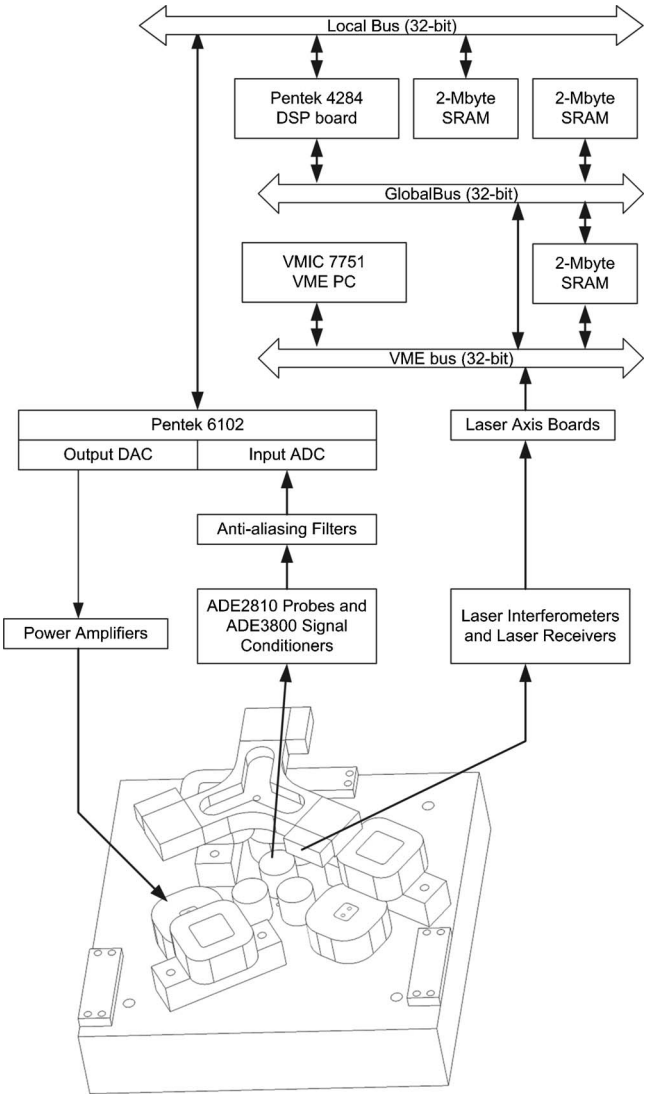

Fig. 5 Instrumentation structure of the maglev stage

(S) magnetic charge on the magnet becomes the following quintuple integration:

$$\mathbf{f} = \frac{J\sigma_m}{4\pi} \int_S \int \int_V \int \int \left(\frac{-(x-p)\hat{\mathbf{k}} + (z-r_1)\hat{\mathbf{i}}}{\{(x-p)^2 + (y-q)^2 + (z-r_1)^2\}^{1.5}} - \frac{-(x-p)\hat{\mathbf{k}} + (z-r_2)\hat{\mathbf{i}}}{\{(x-p)^2 + (y-q)^2 + (z-r_2)^2\}^{1.5}} \right) dydxdzdpdq \tag{2}$$

where $\sigma_m = \pm \mu_0 M$ is the surface magnetic charge density on the top and bottom surfaces of the magnet with permanent magnetization M (A/m). Parameters r_1 and r_2 are the heights of the top and bottom magnet surfaces from the top of the vertical coil. The permeability of free space μ_0 is defined as $4\pi \times 10^{-7}$ H/m, and $\hat{\mathbf{i}}$ and $\hat{\mathbf{k}}$ are the unit vectors in the stationary coordinate frame attached to the coil. The variables x, y, and z are the coordinates of the coil volume segment $dV = dxdydz$, and p and q are those of the magnet area segment $dS = dpdq$. To calculate the vertical force, we divide the coil into four equal sections (viz., 1–4), as shown in Fig. 3. The horizontal force components on Secs. 1 and 3 cancel with the horizontal force components on Secs. 2 and 4 due to their equal magnitudes and opposite directions. The vertical components of these forces are added, and the direction of the resultant force on the vertical coil is downward, so on the magnet, upward.

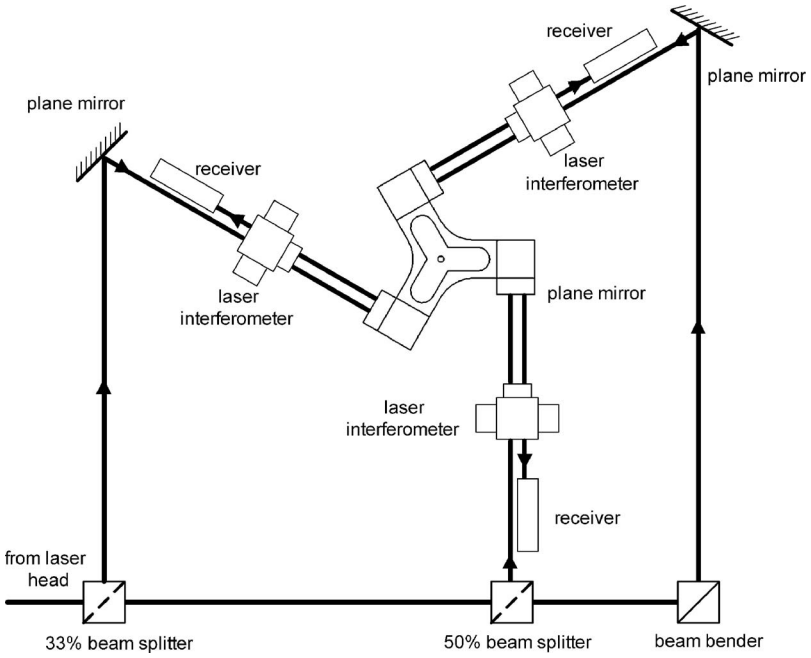

Fig. 6 Laser-interferometry setup of the maglev stage

We multiply a factor of 4 to calculate the overall vertical force.

To find the horizontal force, we calculate the forces F_{h1} and F_{h3} using Eq. (2) (F_{h2} and F_{h4} cancel). We subtract these forces to obtain the equivalent horizontal force on the magnet. These quintuple integrals were evaluated using MATHCAD. It was found to be that there was a reduction in force of around 50% as the height increases from 1 mm to 5 mm. The actuation force decreases as the magnet moves away from the center of the coil. For the horizontal force between the magnet and the horizontal coil, this offset from the center position is small, but the magnitude of the force drops quickly as the magnet moves away from the coil. The calculations show that the force reduces to almost half when the coil is moved from the gap of 0.3–4 mm. Thus, the calculations provide us with a fair estimation of the forces from the horizontal and vertical actuators.

As clearly seen from Eq. (2), these forces are nonlinear functions of the distance between the magnet and the coil. This nonlinearity becomes significant when the actuator operates in large travel ranges. Thus, we incorporated real-time functions to compensate for these nonlinearities. Since the estimated values available to us were at discrete positions, we used the "polyfit" function in MATLAB to fit the force with respect to the distance between the magnet and the coils with a polynomial function. Then we used this polynomial in real time to estimate the currents as a function of the desired forces and the actual distances between the coils and the magnet. The end result of this actuator characterization is presented in Sec. 5.2.

2.3 Actuator Sizing. Actuation force, platen mass, and sensor and actuator packaging were the main design issues, and several design iterations were carried out to determine the optimal sizing of coils and magnets. On the basis of these design iterations, the optimal size of standard square magnets turned out to be $25.4 \times 25.4 \times 12.7$ mm^3. The permanent magnets are neodymium-iron-boron (NdFeB) with the energy product ($BH_{\max}$) of 280 kJ/m^3 (35 MG Oe). The coils were wound with heavy-built AWG (American wire gauge) 24 copper magnet wire that had a layer of heat-bondable epoxy coating on it. For vertical actuators, we have square coils of 10×10 mm^2 inner dimension and 35×35 mm^2 of outer dimension with 679 turns and the resistance of 5.5 Ω. The maximum calculated vertical force is 8.76 N by each vertical actuator at the height of 500 μm. Since there are three such actuators, the total maximum vertical force will be 26.28 N, i.e., 2.68 kgf. The mass of the moving platen is 0.267 kg, so the estimated payload of the stage is more than 2 kg. The inner dimension of the horizontal coil is 20×20 mm^2 and outer dimension is 40×40 mm^2. Each horizontal coil has 561 turns with the resistance of 5.9 Ω. The maximum horizontal force varies from 4.5 N to 2 N for the gap of 0–5 mm between the coil and the magnet.

2.4 Experimental Verification. The magnitude of analytical force was verified using an experimental setup consisting of a precision load cell attached to the magnet and a current-carrying coil below the magnet at a certain height. The load cell was mounted on an $xyz\phi$ stage using a cantilever beam. The value of forces was measured at various heights and offset positions. The forces due to gravity and magnetic attractions were eliminated by subtracting the load-cell reading without any current in the coils from the reading with current. The maximum error between the analytical and experimental values was about 3%, which is reasonable considering the experimental errors in the imprecise measurement of the gap between the coil and the magnet due to uneven surface.

3 Mechanical Design and Assembly

An exploded view of the mechanical assembly is shown in Fig. 4. The Y-shaped part in the center is the single-moving part, the platen. The 3D design of all the parts and the assembly was done using SolidWorks. A finite-element analysis of the platen was carried out to determine its vibration modes and natural frequencies. The dimensions and material properties of all the parts were specified in the SolidWorks model, which was analyzed using COSMOSWorks. Various kinds of restraints were applied on the model, and deformation patterns and natural frequencies were computed. The lowest natural frequency was found to be 680 Hz when the outer face of only one magnet was fixed. Thus, the control bandwidth was kept around 80 Hz, i.e., eight times lower than the natural frequency of the platen to avoid any resonance. Refer to Sec. 5.2 for more on the controller design.

The platen has a simple mechanical design for easy manufac-

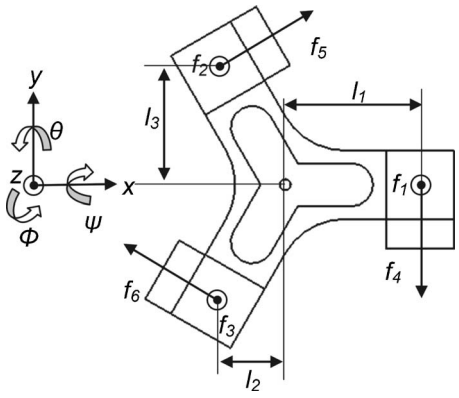

Fig. 7 Allocation of the coordinate axes on the platen for modal force and displacement transformations. The positive directions of ψ, θ, and ϕ follow the right-hand convention.

turing and modeling. It has three cuboid permanent magnets glued at its three ends with epoxy. The square faces on the top and bottom represent N and S poles. A fixture was fabricated and used for precision in the gluing process. There is one vertical coil below and one horizontal coil on the side of each magnet. These coils were glued to the coil holders and mounted on an aluminum base plate with the dimension of $200\times200\times43$ mm^3. This thick base plate with a 16.7 kHz natural frequency is also a good thermal conductor and has a large heat capacity (4.2 kJ/°C), so it dissipates the small heat generated by the coils rapidly preventing any significant structural distortions due to thermal expansion. The bottom surface of the platen is ground to achieve a surface roughness of 2.54 μm since this surface is used as the targets of the capacitance gap sensors. These capacitance sensors measure the height of the platen at three different positions and vertical-axis motions of the platen are calculated by the triangulation using the measured heights at three points. There are three plane mirrors mounted on the side of the magnets for horizontal motion sensing. These plane mirrors act as the reflectors for the laser beams incident from the laser interferometers. Any shift of a mirror in the direction perpendicular to its surface, i.e., along the line of the laser beam, is sensed by a laser receiver.

The mechanism and working principle of this maglev stage is very simple for modeling as well as manufacturing. Compared with our maglev stage presented herein, traditional stages have very complex mechanisms. Several single-axis actuation units were mounted on top of each other to generate multiple-DOF motion. They have several moving parts, which leads to complicated assembly. Several moving parts and joints made the system difficult to model. Furthermore, due to the contact-type nature of the actuators and guiding systems, significant friction and backlash come into play and create errors in precision positioning. However, in our maglev stage, there is just one moving part that has no mechanical contact with any of the stationary parts avoiding friction, stiction, backlash, and hysteresis.

4 Sensor Integration and Instrumentation Structure

A schematic diagram of the instrumentation structure and data flow is shown in Fig. 5. Horizontal position and velocity sensing are performed by laser interferometry. As shown in Fig. 6, three laser interferometers, each facing one of the three plane mirrors, are mounted on the optical table to measure the planar position of the platen. These interferometers use a 6 mm diameter HeNe laser beam of a 632 nm wavelength. Any displacement of the platen along the direction of the laser beam is detected by three laser receivers that send this displacement information to three laser-axis boards (Agilent 10897B) for further processing. They provide

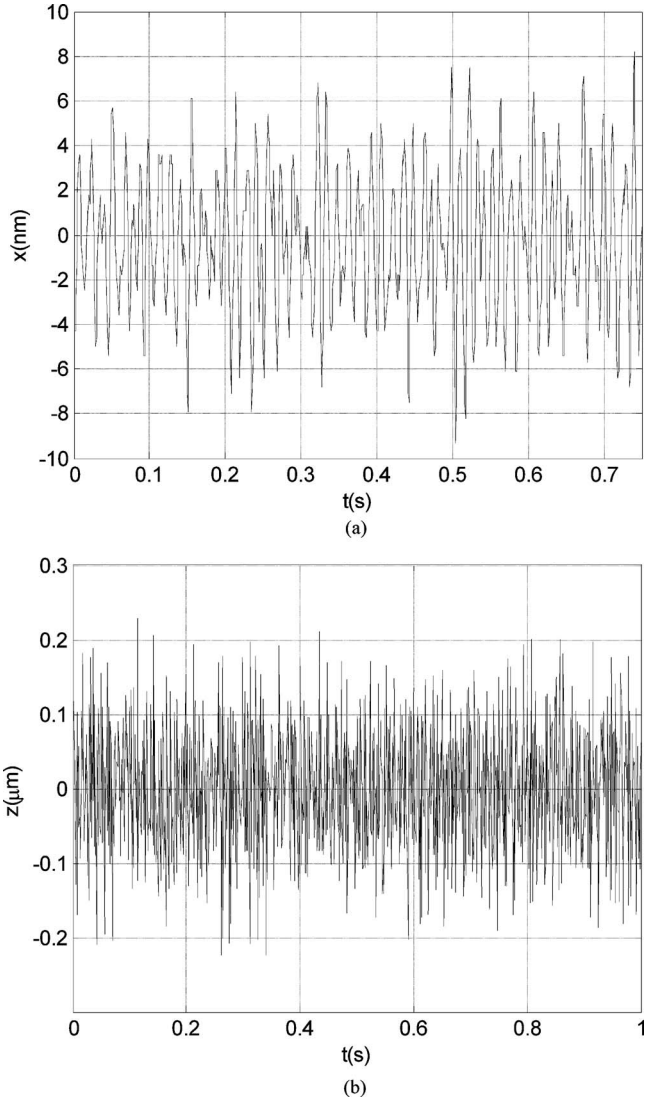

Fig. 8 Position noise in (*a*) *x* and (*b*) *z*

three-axis data (x and y translation and z rotation), and output 35 bit position and 24 bit velocity data at a refresh rate of 10 MHz.

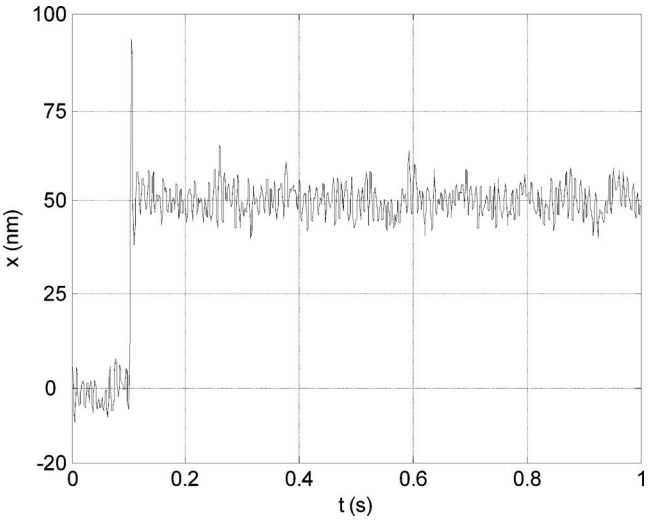

Fig. 9 50 nm step response in *x*

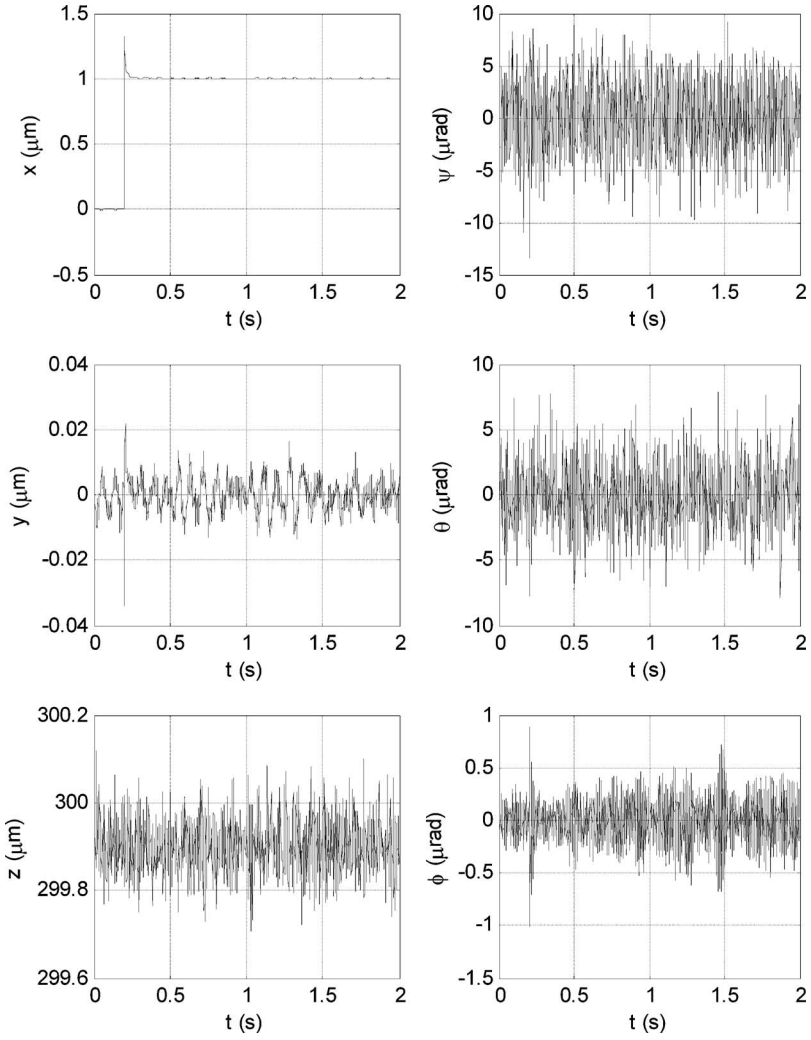

Fig. 10 1 μm step response in the *x* axis with perturbed motions in the other five axes

For vertical motion sensing, we have three capacitance probes (ADE 2810). These sensors are mounted on the base plate right below the platen. They measure the vertical position of the platen at three different points and give the data to their signal conditioners (ADE 3800). The outputs of these signal conditioning boards are passed through a set of first-order low-pass *RC* antialiasing filters with a cutoff frequency of 1 kHz. The 16 bit ADCs on a data acquisition board (Pentek 6102) are used to digitize the sensor data. A Versa Module Eurocard (VME) bus is used for the communication between various electronic devices. The three laser-axis boards and the data acquisition board are mounted on a VME chassis. The six-axis position data and three-axis velocity data are made available to a digital signal processor (DSP) board (Pentek 4284). The TMS320C40 DSP executes the real-time control code written in C. It collects all the position data available from the sensor boards and performs a modal displacement transformation to calculate the actual position and velocity of the platen center of mass. It acquires the desired position of the platen from the user and applies the control law. Then the DSP board calculates the output to each axis and sends it to digital-to-analog converters (DACs) available on Pentek 6102. This cycle is repeated with an interrupt service routine (ISR) initiated by a hardware interrupt at a sampling frequency of 5 kHz. The output voltages of the DACs are given to six linear transconductance amplifiers with gain of 0.5 A/V. The outputs of the amplifiers are connected to the corresponding coils via twisted shielded cables to avoid picking up external noise. The coils generate the magnetic fields that interact with the magnets and apply forces on the platen causing motion.

5 Dynamic Modeling and Control

5.1 Plant Modeling. A 3D model of the whole maglev system was developed with SolidWorks, and a finite-element analysis was carried out to identify various system parameters such as mass, moment of inertia, and center of mass. The system has just one moving part levitated by magnetic forces on the magnets attached to it. In the absence of any mechanical contact with the stationary parts, we assume that magnetic spring and damping effects are negligible. Thus, we model this plant as a pure mass, and the equation of translational motion of the platen is

$$M\frac{d^2x}{dt^2} = f \tag{3}$$

where M is the mass of the platen, i.e., 0.267 kg, and f is the corresponding modal force. Thus, the transfer function of the platen for translation in x is

$$\frac{X(s)}{F(s)} = \frac{1}{0.267s^2} \tag{4}$$

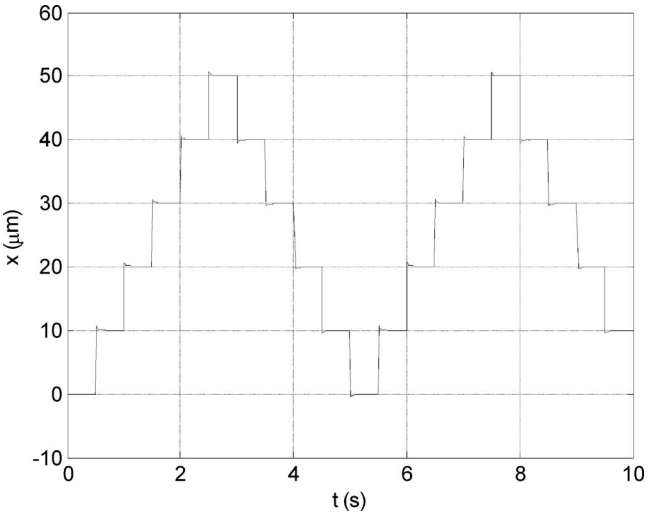

Fig. 11 10 μm consecutive steps in *x*

Similarly, the transfer function of the platen for rotation about the y axis is

$$\frac{\Theta(s)}{T(s)} = \frac{1}{I_{yy}s^2} \tag{5}$$

where I_{yy} is the principal moment of inertia about the y axis, and T refers to the torque about that axis. The inertia matrix, taken at the platen center of mass, obtained using SolidWorks (the allocation of the coordinate axes is shown in Fig. 7) is given by

$$I = \begin{bmatrix} I_{xx} & -I_{xy} & -I_{xz} \\ -I_{yx} & I_{yy} & -I_{yz} \\ -I_{zx} & -I_{zy} & I_{zz} \end{bmatrix} = \begin{bmatrix} 340.37 & 0 & 0 \\ 0 & 340.37 & 0 \\ 0 & 0 & 653.61 \end{bmatrix} \tag{6}$$

with units in 10^{-6} kg m^2. The principal moments of inertia of the platen are equal along the two horizontal axes and all product-of-inertia terms are zero. Hence, theoretically, there is no dynamic coupling between the motions in all the three rotational axes. This is due to the innovative symmetrical design of the moving platen, facilitating the simplicity in modeling and control along with easy manufacturing.

Translations and rotations in various axes are achieved by combinations of forces generated by the six linear actuators. The modal force transformation was determined to be

$$\begin{bmatrix} f_x \\ f_y \\ \tau_\phi \\ f_z \\ \tau_\psi \\ \tau_\theta \end{bmatrix} = \begin{bmatrix} 0 & 0 & 0 & 0 & \cos 30\ \text{deg} & -\cos 30\ \text{deg} \\ 0 & 0 & 0 & -1 & \sin 30\ \text{deg} & \sin 30\ \text{deg} \\ 0 & 0 & 0 & -l_1 & -l_1 & -l_1 \\ 1 & 1 & 1 & 0 & 0 & 0 \\ 0 & l_3 & -l_3 & 0 & 0 & 0 \\ -l_1 & l_2 & l_2 & 0 & 0 & 0 \end{bmatrix} \begin{bmatrix} f_1 \\ f_2 \\ f_3 \\ f_4 \\ f_5 \\ f_6 \end{bmatrix} \tag{7}$$

where f_x, f_y, and f_z are the modal forces, and τ_ψ, τ_θ, and τ_ϕ are the modal torques about the x, y, and z axes, respectively. The definitions of forces and distances are shown in Fig. 7. The lengths of physical dimensions, l_1, l_2, and l_3 are defined as follows: l_1, distance between the mass centers of the magnets and the platen center=0.05059 m; l_2, distance between the mass centers of Magnets 2 or 3 and the platen center along the x axis=0.02529 m; l_3, distance between the mass centers of Magnets 2 or 3 and the platen center along the y axis=0.04382 m.

To calculate the six-axis position of the platen, we use data from the six sensors. For the horizontal motion sensing, we use the three-axis displacements measured by the laser interferometers and take the inverse of the geometric relation of

$$\begin{bmatrix} L_1 \\ L_2 \\ L_3 \end{bmatrix} = \begin{bmatrix} 0 & -1 & l_1 \\ \cos 30\ \text{deg} & \cos 60\ \text{deg} & l_1 \\ -\cos 30\ \text{deg} & \cos 60\ \text{deg} & l_1 \end{bmatrix} \begin{bmatrix} x \\ y \\ \phi \end{bmatrix} \tag{8}$$

that yields

$$\begin{bmatrix} x \\ y \\ \phi \end{bmatrix} = \begin{bmatrix} 0 & 0.5774 & -0.5774 \\ -0.6667 & 0.3333 & 0.3333 \\ 6.5928 & 6.5928 & 6.5928 \end{bmatrix} \begin{bmatrix} L_1 \\ L_2 \\ L_3 \end{bmatrix} \tag{9}$$

where L_1, L_2, and L_3 are the readings from the three laser interferometers, respectively.

For the vertical motions, we use the three heights measured by the capacitance probes and take the inverse of the geometric relations of

$$\begin{bmatrix} C_1 \\ C_2 \\ C_3 \end{bmatrix} = \begin{bmatrix} 1 & 0 & -d_1 \\ 1 & d_3 & d_2 \\ 1 & -d_3 & d_2 \end{bmatrix} \begin{bmatrix} z \\ \psi \\ \theta \end{bmatrix} \tag{10}$$

that yields

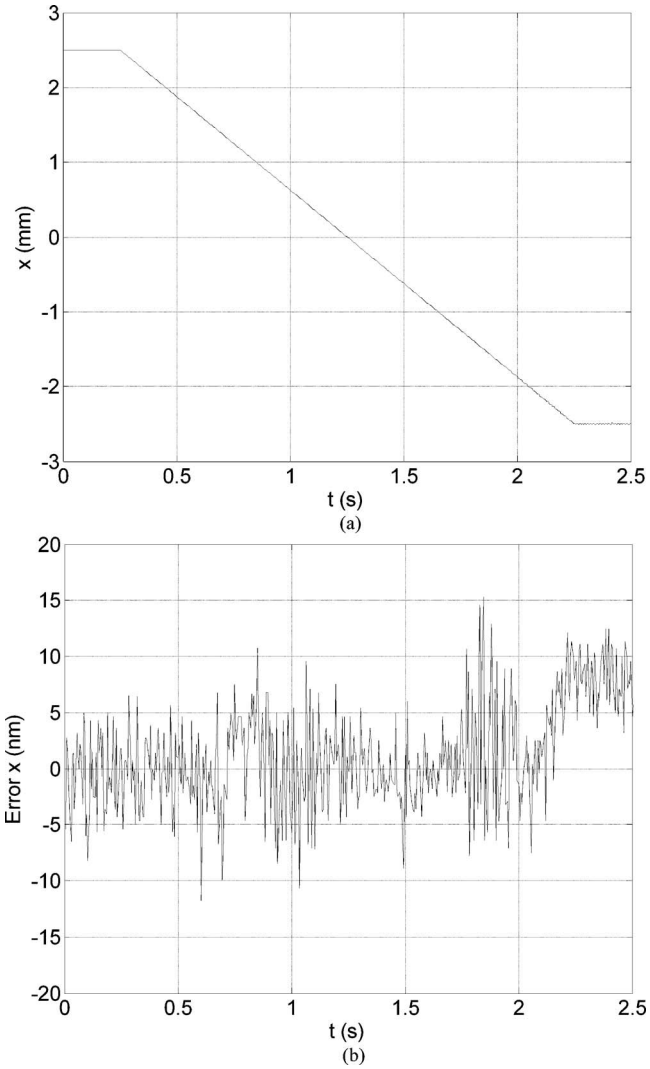

Fig. 12 (*a*) 5 mm ramp motion in *x* and (*b*) position error in *x* in this motion

$$\begin{bmatrix} z \\ \psi \\ \theta \end{bmatrix} = \begin{bmatrix} 0.3333 & 0.3333 & 0.3333 \\ 0 & 40.0128 & 40.0128 \\ -46.2000 & 23.1000 & 23.1000 \end{bmatrix} \begin{bmatrix} C_1 \\ C_2 \\ C_3 \end{bmatrix} \tag{11}$$

where C_1, C_2, and C_3 are the readings from the three capacitance sensors, respectively, and the distances, d_1, d_2, and d_3 are defined as follows: d_1, distance between the origin of the stationary coordinate system and C_1 along the x axis=0.01443 m; d_2, distance between the origin of the stationary coordinate system and the center of C_2 and C_3 along the x axis=0.007215 m; d_3, distance between the origin of the stationary coordinate system and the center of C_2 and C_3 along the y axis=0.012496 m.

Thus, the modal displacement transformation was derived to resolve the six-axis modal position of the platen mass center from the raw sensor data.

$$\begin{bmatrix} x \\ y \\ \phi \\ z \\ \psi \\ \theta \end{bmatrix} = \begin{bmatrix} 0 & 0.5774 & -0.5774 & 0 & 0 & 0 \\ -0.6667 & 0.3333 & 0.3333 & 0 & 0 & 0 \\ 6.5928 & 6.5928 & 6.5928 & 0 & 0 & 0 \\ 0 & 0 & 0 & 0.3333 & 0.3333 & 0.3333 \\ 0 & 0 & 0 & 0 & 40.0128 & -40.0128 \\ 0 & 0 & 0 & -46.2 & 23.1 & 23.1 \end{bmatrix} \times \begin{bmatrix} L_1 \\ L_2 \\ L_3 \\ C_1 \\ C_2 \\ C_3 \end{bmatrix} \tag{12}$$

Using the modal force and displacement transformations and the dynamic model of the platen, we designed a closed-loop controller for the maglev stage.

5.2 Control System Design. A decoupled lead-lag controller was designed on the basis of the dynamic model derived in the previous section. A free pole was placed at the origin of the s-plane to eliminate steady-state position error. The controller given below has a phase margin of 70 deg at a crossover frequency of 80 Hz.

$$G(s) = \frac{K(s+116.6)(s+10.9)}{s(s+4013.9)} \tag{13}$$

where K is the gain of the controller, which is 7.37×10^5 N/m for x, y, and z translation. For rotation, the values of K are 939.54 N/rad, 939.54 N/rad, and 1804.16 N/rad for ψ, θ, and ϕ, respectively. We used the zero-order-hold (ZOH) equivalence method to convert this continuous-time controller to a discrete-time one at a 5 kHz sampling frequency and implemented it on the DSP as a difference equation [13].

The nonlinearity of the force constant was discussed in Sec. 2. Since this maglev stage has a large travel range, this nonlinearity cannot be ignored. We calculated force at several heights and analyzed the polynomial function of the force with respect to the gap (d), as described in Sec. 2. For horizontal motion, this nonlinear function turned out to be

$$F(i,d) = (0.01303d^2 - 0.2716d + 2.205)i \tag{14}$$

where d is the gap between the magnet and the coil in millimeters, and i is the coil current in amperes. Since we know the gap between the coil and the magnet at every instant by sensor measurement, we can use the above equation to calculate the required current in the coil precisely for the desired force on the magnet in real time.

6 Experimental Results

We implemented the controller designed in the previous section and performed various experiments to test the positioning capability of the stage. Figure 8(a) shows a position noise profile in the x axis while the platen is levitated. The peak-to-peak noise is less than 18 nm, i.e., the noise level is around 3 nm rms in the horizontal directions. The nominal gap of levitation varies between 250 μm and 750 μm and this motion is limited due to the linear sensing range of the capacitance sensors. The noise in the vertical direction (z) is shown in Fig. 8(b). The peak-to-peak noise in the z axis is around 0.4 μm. The analog sensor data for vertical motion must be digitized by an ADC. The cumulative effect of sensor noise, ADC noise, and ADC quantization makes the vertical motion profile noisier. Despite the noise in the vertical axes, the horizontal motion profile is very quiet. This indicates that there is little dynamic coupling between the horizontal and vertical motions of the maglev stage and that the horizontal controller is robust enough to reject any noise from the vertical motion.

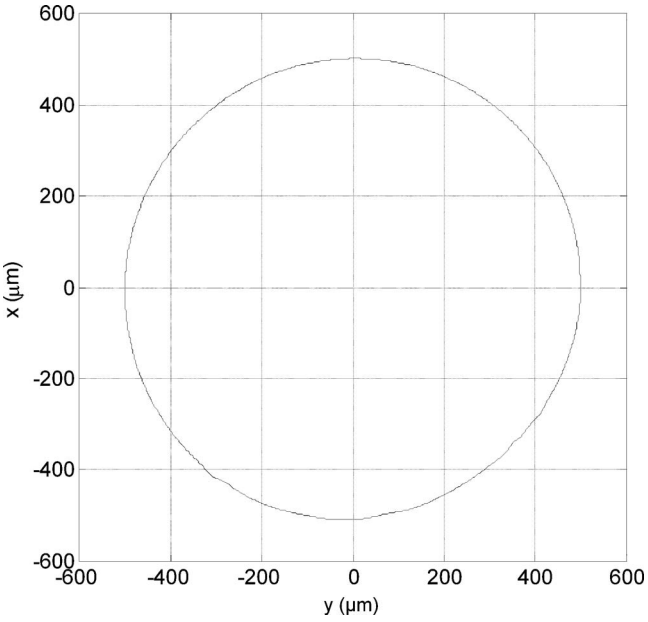

Fig. 13 500 μm radius circular motion in the *x-y* plane

Figure 9 shows a 50 nm step response in the x axis. The position noise level is again maintained under 3 nm rms. Figure 10 shows a 1 μm step response in the x axis with the perturbation motions in the other five axes. It is evident that due to coupling of the motions among the horizontal axes, there are some spikes in the y- and ϕ-axis motions. The noise in the y axis increases right after the step but settles back to 20 nm peak to peak. Figure 11 shows 10 μm consecutive step responses at the interval of 0.5 s in the x axis. The platen moves to the desired position without large overshoot and settles down fast and responds to the next step command. Figure 12(a) shows a ramp motion of 5 mm in the x axis demonstrating the large travel range of the maglev stage. Figure 12(b) shows the tracking error (commanded position minus measured position). Figure 13 shows a 500 μm radius circular path traversed by the platen in the x-y plane. The motion of the platen is very close to a perfect circle.

Potential applications of this maglev stage include positioning stages for μSTL and nanoindentation. Figure 14 shows a path in the shape of a spur gear traversed by the platen. Its inner radius is 500 nm and outer radius is 675 nm. This proves the nanoscale positioning capability of the maglev stage. Figure 15 shows a 3D path traversed by the platen in the area of 80×60 μm^2. While generating the scanning path, the stage took up/down steps in the z axis from 195 μm to 200 μm. There are two different markers used here. The triangular markers show the points above 198 μm and the dots, points below 198 μm. If a stiff AFM tip is fixed to the base and a silicon substrate is attached to the moving platen,

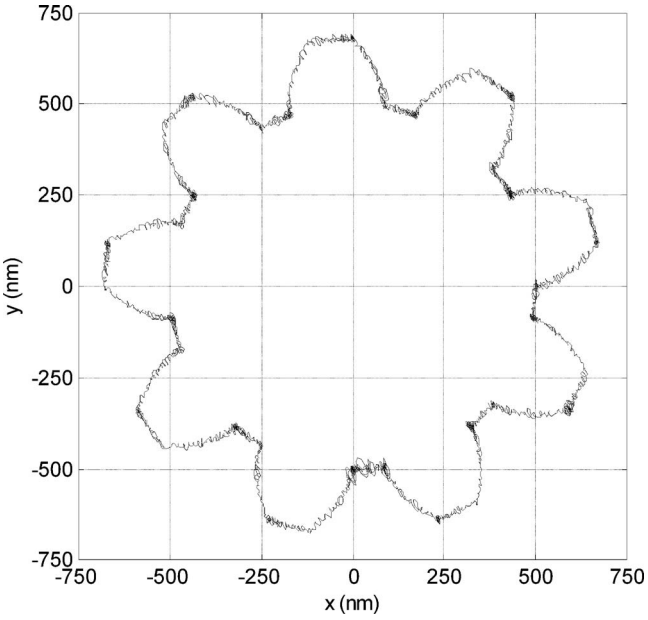

Fig. 14 Path in a shape of a spur gear of 500 nm inner radius and 675 nm outer radius in the *x-y* plane

the tip will make indents/scratches and we can write small letters or draw tiny shapes on the silicon substrate. These positioning capabilities imply the versatile applications of this maglev stage.

7 Conclusions

In this paper, we presented a novel maglev stage with an extended travel range of 5×5 mm^2 in the x and y axes and 500 μm in the z axis. The z axis travel range is limited by the capacitance-sensor specifications. However, we sized the vertical actuators so that this stage would have a travel range of 5 mm in the z axis as well with long-range sensors. The stage has noise level of 4 nm rms with maximum acceleration of 8 g in vertical and 2.5 g in horizontal directions, respectively. It is capable of precisely orienting and positioning an additional payload of 2 kg. The maglev stage has a very simple mechanical structure with a single-moving part, which is easy and inexpensive to fabricate.

We discussed the novel dual-axis actuation scheme and the design of the actuators. An extensive electromagnetic analysis of the actuator forces over the whole travel range was carried out. Experimental results confirmed the analysis with only a 4% maximum error. A dynamic model of the maglev system and modal force and displacement transformations were derived. The design and implementation of lead-lag controllers was successfully accomplished.

Applications of this maglev stage include nanomanipulation, fabrication, and handling of nanosized objects, 3D rapid prototyping of microsized objects, and vibration isolation for delicate instrumentation. Several single and multiaxis experimental results demonstrated that maglev stage could be used as a positioner for μSTL and nanoindentation applications. In summary, this maglev stage is a promising solution to nanopositioning requirements of the next-generation nanotechnology.

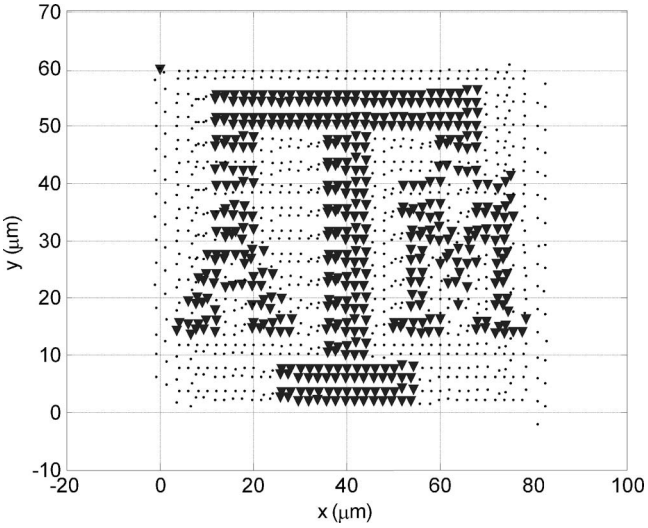

Fig. 15 The logo of Texas A&M University plotted over an area of 80×60 μm^2 in the *x-y* plane

Acknowledgment

This material is based on the work supported by the National Science Foundation under the Grant No. CMS-0116642.

References

[1] Binnig, G., Quate, C. F., and Gerber, C. H., 1986, "Atomic Force Microscope," Phys. Rev. Lett., **56**(9), pp. 930–933.
[2] Taylor, R. M., II, 1994, "The Nanomanipulator: A Virtual-Reality Interface to a Scanning Tunneling Microscope," Ph.D. thesis, University of North Carolina at Chapel Hill, NC.
[3] Smith, S., and Chetwynd, D., 1963, *Microscopic Staining Techniques*, Butterworths, London.
[4] Jung, K. S., and Baek, Y. S., 2002, "Study on a Novel Contact-Free Planar System Using Direct Drive dc Coils and Permanent Magnets," IEEE/ASME Trans. Mechatron., **7**(2), pp. 35–43.
[5] Kim, W.-J., and Trumper, D. L., 1998, "High-Precision Magnetic Levitation Stage for Photolithography," Precis. Eng., **22**(2), pp. 66–77.
[6] Kim, W.-J., 1997, "High-Precision Planar Magnetic Levitation," Ph.D. thesis, Massachusetts Institute of Technology, Cambridge, MA.
[7] Hollis, R. L., Salcudean, S. E., and Allan, A. P., 1991, "A Six Degree-of-Freedom Magnetically Levitated Variable Compliance Fine-Motion Wrist: Design Modeling, and Control," IEEE Trans. Rob. Autom., **7**(3), pp. 320–332.
[8] Chen, M. Y., Wang, M. J., and Fu, L. C., 2003, "A Novel Dual-Axis Repulsive Maglev Guiding System With Permanent Magnet: Modeling and Controller Design," IEEE/ASME Trans. Mechatron., **8**(1), pp. 77–86.
[9] Chen, M. Y., Tsai, C. F., Huang, H. H., and Fu, L. C., 2005, "Integrated Design of a Planar Maglev System for Micro Positioning," *Proceedings of American Control Conference*, pp. 3066–3071.
[10] Jung, C. G., 1996, "A Six Degree-of-Freedom, Magnetica Levitation-Driven, Automated System for Nondestructive Tab Inner Lead Bond Quality Test," Ph.D. thesis, University of Texas at Austin, TX.
[11] Gu, J., Kim, W.-J., and Verma, S., 2005, "Nanoscale Motion Control With a Compact Minimum-Actuator Magnetic Levitator," Journal of Dynamic Systems, J. Dyn. Syst., Meas., Control, **127**(3), pp. 433–442.
[12] Verma, S., Kim, W.-J., and Gu, J., 2004, "6-Axis Nanopositioning Device With Precision Magnetic Levitation Technology," IEEE/ASME Trans. Mechatron., **9**(2), pp. 384–391.
[13] Franklin, G. F., Powell, J. D., and Emami-Naeini, A., 2001, *Feedback Control of Dynamic Systems*, 4th ed., Prentice-Hall, Eaglewood Cliffs, NJ.